OPEN ACCESS



GeV Signatures of Short Gamma-Ray Bursts in Active Galactic Nuclei

Chengchao Yuan b, Kohta Murase c, Dafne Guetta, Asaf Pe'er b, Imre Bartos, and Péter Mészáros bepartment of Physics, Department of Astronomy & Astrophysics, Center for Multimessenger Astrophysics, Institute for Gravitation and the Cosmos, The Pennsylvania State University, University Park, PA 16802, USA; cxy52@psu.edu, murase@psu.edu

Center for Gravitational Physics, Yukawa Institute for Theoretical Physics, Kyoto University, Kyoto, Kyoto 606-8502, Japan

Department of Physics, Ariel University, Ariel, Israel

Department of Physics, Bar-Ilan University, Ramat-Gan 52900, Israel

Department of Physics, University of Florida, PO Box 118440, Gainesville, FL 32611-8440, USA

Received 2021 December 16; revised 2022 April 3; accepted 2022 May 5; published 2022 June 17

Abstract

The joint detection of gravitational waves and the gamma-ray counterpart of a binary neutron star merger event, GW170817, unambiguously validates the connection between short gamma-ray bursts and compact binary object (CBO) mergers. We focus on a special scenario where short gamma-ray bursts produced by CBO mergers are embedded in disks of active galactic nuclei (AGNs), and we investigate the γ -ray emission produced in the internal dissipation region via synchrotron, synchrotron self-Compton, and external inverse Compton (EIC) processes. In this scenario, isotropic thermal photons from the AGN disks contribute to the EIC component. We show that a low-density cavity can be formed in the migration traps, leading to the embedded mergers producing successful GRB jets. We find that the EIC component would dominate the GeV emission for typical CBO mergers with an isotropic-equivalent luminosity of $L_{j,\rm iso} = 10^{48.5}~{\rm erg~s}^{-1}$ that are located close to the central supermassive black hole. Considering a long-lasting jet of duration $T_{\rm dur} \sim 10^2 - 10^3~{\rm s}$, we find that the future Cherenkov Telescope Array (CTA) will be able to detect its 25–100 GeV emission out to a redshift z=1.0. In the optimistic case, it is possible to detect the on-axis extended emission simultaneously with GWs within one decade using MAGIC, H.E. S.S., VERITAS, CTA, and LHAASO-WCDA. Early diagnosis of prompt emissions with Fermi-GBM and HAWC can provide valuable directional information for the follow-up observations.

Unified Astronomy Thesaurus concepts: Gamma-ray bursts (629); Active galactic nuclei (16); Non-thermal radiation sources (1119); Compact binary stars (283)

1. Introduction

As one of the most luminous and energetic phenomena in the universe, gamma-ray bursts (GRBs) have fueled a vibrant field of astrophysics research for several decades. Based on the duration of the bursts, the population can be divided into two subclasses, long GRBs and short GRBs, which are thought to arise from different progenitors. The general view is that short GRBs result from compact binary object (CBO) mergers (e.g., Paczynski 1986; Eichler et al. 1989; Meszaros & Rees 1992; Narayan et al. 1992; Lee & Ramirez-Ruiz 2007; Berger 2014), such as binary neutron star (NS) mergers and potentially NSblack hole (BH) mergers, whereas long GRBs are generated during the death of massive stars (e.g., Woosley 1993; Paczyński 1998; MacFadyen & Woosley 1999; Popham et al. 1999; Mészáros 2006; Hjorth & Bloom 2012). In 2017, the coincident detection of gravitational waves (GWs) and the corresponding electromagnetic counterpart from the binary NS merger GW170817, located in the host galaxy NGC 4933, marked a triumph of multimessenger astronomy (Abbott et al. 2017a, 2017b, 2017c, 2017d). The spatial and temporal association between GW170817 and GRB 170817A also consolidates the theory that CBO mergers are the origin of short GRBs. Extensive efforts have shown that the broadband emission is consistent with a relativistic jet viewed from an off-axis angle (Abbott et al. 2017b; Goldstein et al. 2017;

Original content from this work may be used under the terms of the Creative Commons Attribution 4.0 licence. Any further distribution of this work must maintain attribution to the author(s) and the title of the work, journal citation and DOI.

Hallinan et al. 2017; Savchenko et al. 2017; Troja et al. 2017; Lazzati et al. 2018; Lyman et al. 2018; Mooley et al. 2018a, 2018b; Gottlieb et al. 2019; Ioka & Nakamura 2019). Moreover, Kimura et al. (2019) investigated the upscattered cocoon emission as the source of the γ -ray counterpart. The long-lasting high-energy signatures of the central engine left after the coalescence was studied in Murase et al. (2018).

Alternatively, unlike in the case of GW170817, one can expect a subpopulation of short GRBs that occur in the accretion disks of AGNs. Studies of the CBO formation and evolution in AGN disks demonstrate that hierarchical mergers of embedded binary BH (BBH) systems are promising for reconstructing the parameters of LIGO/VIRGO-detected mergers (Gayathri et al. 2020; Samsing et al. 2020; Bartos 2021; Tanikawa et al. 2021). These mergers can harden the BH mass distribution (Yang et al. 2019b, 2019a; Tagawa et al. 2020, 2021) as well. Yang et al. (2020) pointed out that mergers involving NSs, such as GW190814 and GW190425, could also arise in AGN disks. Recent progress on the optical counterpart to GW190521 could support this (Graham et al. 2020), although the confirmation needs further observations (Ashton et al. 2021). Perna et al. (2021) systematically studied the electromagnetic signatures of both long GRBs and short GRBs in AGN disks and discussed the conditions for shock breakout. Zhu et al. (2021a) and Zhu et al. (2021b) focused more on the neutrino production of embedded explosions. However, Kimura et al. (2021) showed that CBO environments are likely to be thin because of outflows that are common in super-Eddington accretion.

In this work, we study γ -ray emission from short GRBs that are embedded in AGN disks. Inside the accretion disk, the

embedded objects can migrate toward a migration trap owing to angular momentum exchange via the torques originating from the disk density perturbations. At the migration trap, the gas torque changes sign, and an equilibrium is achieved as the outwardly migrating objects meet inwardly migrating objects. Numerical calculations show that compact binaries are typically formed near the migration trap at distances around $R_d \sim (20-300)R_S$ to the central supermassive BH (SMBH; Bellovary et al. 2016), where $R_S = 2GM_{\star}/c^2$ is the Schwarzschild radius. Employing one-dimensional N-body simulations, Tagawa et al. (2020) obtained a more distant location for typical mergers at $\sim 10^{-2}$ to 10^{-1} pc ($\sim (10^3 - 10^4) R_{\rm S}$ for an SMBH with mass $M_{\star} = 10^8~M_{\odot}$). We concentrate on the embedded GRBs with distances $R_d \sim (10-10^3)R_S$. We will show that AGN disks would not influence the γ -ray emission if the CBO mergers happen farther outside in the disk. We also note that $R_d = 10R_S$ is an extreme case where the population is stringently limited. The outflows from the binary systems with super-Eddington accretion rates are expected to form a lowdensity cavity-like structure before the merger occurs (Kimura et al. 2021). Within such a cavity a successful GRB jet is likely to develop, since the ambient gas density is not sufficiently high to stall the jet, in contrast to the choked-jet case discussed in Zhu et al. (2021b).

In GRB theories, EIC processes can be important when seed photons in the external regions or late/early-time dissipation processes can be efficiently upscattered to the GeV–TeV bands by accelerated electrons (e.g., Murase et al. 2011; Veres & Mészáros 2012; Kimura et al. 2019). The EIC scenario can be used to explain the observed very high energy (VHE) emission from GRBs (e.g., Zhang et al. 2021a, 2021b). In the present case, the disk blackbody emission provides an appropriate supply of thermal photons to the short GRB jets.

Adopting a thin-disk model, we derive the conditions for cavity formation and calculate disk photon spectra in Section 2. In Section 3, we numerically solve the steady-state transport equation to obtain the electron distribution inside the jet. In Section 4, we calculate the synchrotron, synchrotron self-Compton (SSC), and EIC components. The effects of $\gamma\gamma$ absorption in the AGN disk and electromagnetic cascades are also taken into account. We also present the detection perspectives for the Fermi Large Area Telescope (Fermi-LAT) and the VHE γ -ray facilities, such as the Major Atmospheric Gamma Imaging Cherenkov (MAGIC), the High Energy Stereoscopic System (H.E.S.S.), the Very Energetic Radiation Imaging Telescope Array System (VERITAS), the Cherenkov Telescope Array (CTA), and the water Cherenkov detector array in the Large High Altitude Air Shower Observatory (LHAASO-WCDA), in Section 4.2. The prompt emissions are discussed in Section 4.3. We summarize and discuss the results in Section 5.

Throughout the paper, we use the notation $Q_x = Q/10^x$, and physical quantities are written in CGS units unless otherwise specified. Quantities with the prime symbol, e.g., Q', are written in the jet comoving frame. We use the symbol F[a, b, c, ...] to represent the value of a function F evaluated at the point (a, b, c, ...).

2. Cavity Formation and Disk Photon Spectra

In this section we derive the conditions for the formation of a low-density cavity around the CBO, following the treatment in Kimura et al. (2021), and model the AGN disk temperature distribution assuming a steady thin disk.

2.1. Cavity Formation

For a thin AGN disk with an aspect ratio $h_{AGN} =$ $H_{\rm AGN}/R_d \sim 0.01$ surrounding an SMBH with mass $M_{\star} =$ $10^8 M_{\star,8}$ M_{\odot} , we write down the accretion rate onto the SMBH and the radial drift velocity v_R as, respectively, Which and the factor difference of the AGN disk, $\dot{M}_{\star} = \dot{m}_{\star} L_{\rm Edd,\star}/c^2 \simeq 1.4 \times 10^{25} \, \dot{m}_{\star} \dot{M}_{\star,8} \, {\rm g \ s^{-1}}$ and $v_R = v/R_d \approx \alpha h_{\rm AGN}^2 v_K \simeq 2.1 \times 10^4 \, \alpha_{-1} h_{\rm AGN,-2}^2 \mathcal{R}_2^{-1/2} \, {\rm cm \ s^{-1}}$ (Frank et al. 2002), where $H_{\rm AGN}$ is the scale height of the AGN disk, $\alpha \sim 0.1$ is the viscous parameter, ν is the kinematic viscosity, $v_{\rm K} = \sqrt{GM_{\star}/R_d}$ is the Kepler velocity, R_d is the distance between the CBO and the central SMBH, the dimensionless parameter \mathcal{R} is defined as $\mathcal{R} \equiv R_d/R_S$, and $L_{\text{Edd},\star}$ stands for the Eddington luminosity. The surface density for a stable disk can then be written as $\Sigma_{\rm AGN} = \dot{M}_{\star}/(2\pi R_d v_R) \simeq 3.6 \times 10^4 \ \dot{m}_{\star} M_{\star,8} \mathcal{R}_2^{-1/2} \alpha_{-1}^{-1} h_{\rm AGN,-2}^{-2} \ {\rm g \ cm^{-2}}$. When a CBO is present in the AGN disk, the surface density is perturbed, and a density gap will appear bracketing the binary's orbit around the SMBH (Kanagawa et al. 2015). For a typical short GRB progenitor, we expect the total mass of the binary system to be $M_{\rm CBO} \lesssim 10$ M_{\odot} . In this case $\Sigma_{\rm CBO} \approx \Sigma_{\rm AGN}$ is a good approximation to the surface density of the AGN disk at the binary's position (Kimura et al. 2021). We obtain the disk gas density in the vicinity of the CBO,

$$\rho_{\text{CBO}} = \frac{\Sigma_{\text{CBO}}}{2H_{\text{AGN}}} \simeq 6.1 \times 10^{-10} \,\dot{m}_{\star} M_{\star,8} \times \mathcal{R}_{2}^{-3/2} \alpha_{-1}^{-1} h_{\text{AGN},-2}^{-3} \,\text{g cm}^{-3},$$
 (1)

and the disk magnetic field,

$$B_d = \sqrt{8\pi\beta^{-1}(\rho_{\text{CBO}}/m_p)k_BT_d}$$

$$\simeq 2.1 \times 10^2 \,\beta_{0.48}^{-1/2} \dot{m}_{\star}^{1/2} M_{\star,8}^{1/2} R_2^{-3/4} \alpha_{-1}^{-1/2}$$

$$\times h_{\text{AGN}-2}^{-3/2} T_d^{1/2} \,\text{G}, \tag{2}$$

where $\beta \sim 3$ –30 is defined as the ratio of the plasma pleasure to the magnetic pressure and T_d is the disk temperature. Henceforth, the sub-index "CBO" will be used to stand for quantities describing CBOs.

We estimate the accretion rate of the CBO to be $\dot{M}_{\rm CBO} \approx \eta_{\rm CBO} \dot{M}_{\star} \simeq 1.4 \times 10^{24} \, \dot{m}_{\star} M_{\star,8} \eta_{\rm CBO,-1} \, {\rm erg \ s^{-1}},$ where $\eta_{\rm CBO}$ is the ratio of the CBO accretion rate to the SMBH accretion rate. This approximation is justified in Kimura et al. (2021). We find that the accretion is highly super-Eddington, e.g., $\dot{m}_{\rm CBO} = \dot{M}_{\rm CBO} c^2 / L_{\rm Edd,CBO} \simeq 10^6 \dot{m}_{\star} M_{\star,8} M_{\rm CBO,1}^{-1} \eta_{\rm CBO,-1},$ and expect a wind bubble to be produced by the strong radiation-driven outflows (e.g., Ohsuga et al. 2009; Jiang et al. 2014; Sadowski et al. 2014). The bubble's expansion in a uniform medium can be described by the formula $r_B \approx 0.88 (L_w t^3 / \rho_{\rm CBO})^{1/5}$ (e.g., Weaver et al. 1977; Koo & McKee 1992), where r_B is the bubble radius, $L_w = \eta_w \dot{M}_{\rm CBO} v_w^2 \simeq 1.4 \times 10^{42} \, \dot{m}_{\star} M_{\star,8} \eta_{\rm CBO,-1} \eta_w v_{w,9}^2 \, {\rm erg \ s^{-1}},$ and $v_w \sim 10^9 v_{w,9} \, {\rm cm \ s^{-1}}$ is the outflow velocity. Since the accretion is highly super-Eddington, the factor η_w can reach $\sim 90\%$ –100% (Jiao et al. 2015; Kitaki et al. 2018). However, we use a conservative value $\eta_w \sim 0.3 \, \eta_{w,-0.5}$ (Jiang et al. 2014). Equating the bubble radius r_B to $H_{\rm AGN} / \cos \psi$, we obtain the timescale to create a cavity reaching the approximate boundary

of the AGN disk along the direction of the GRB jet,

$$t_{\text{cav}} \approx 1.2 \left(\frac{\rho_{\text{CBO}} H_{\text{AGN}}^5}{L_w \cos^5 \psi} \right)^{1/3}$$

$$\approx 4.0 \times 10^5 (\cos \psi)^{-5} \mathcal{R}_2^{7/6} \alpha_{-1}^{-1/3} h_{\text{AGN},-2}^{2/3}$$

$$\times \eta_{\text{CBO}-1}^{-1/3} \eta_{w-0}^{-1/3} s v_{w,9}^{-2/3} s, \qquad (3)$$

where ψ is the angle between binary orbital plane and the AGN disk (see the schematic picture in Figure 1). One caveat is that we assumed a spherical outflow to derive the cavity timescale, Equation (3). Sadowski et al. (2014) pointed out that the outflow is concentrated in a wide-angle funnel that surrounds the jet if the accretion rate is highly super-Eddington. In the following text, we will continue using the spherical cavity timescale for simplicity to obtain sufficient conditions for the cavity formation.

The formation of a cavity for a CBO located at R_d before the merger occurs requires

$$t_{\rm cav} \lesssim \min[t_{\rm gw}, t_{\rm mig}, t_{\rm vis}],$$
 (4)

where $t_{\rm gw}$, $t_{\rm mig}$, and $t_{\rm vis}$ are binary merger, migration, and AGN disk viscosity timescales, respectively. We write down the timescales for an equal-mass binary explicitly as

$$t_{\rm gw} = \frac{5}{128} \frac{\dot{m}_{\rm CBO}^4}{A_{\rm in}^4} \frac{GM_{\rm CBO}}{c^3}$$

$$\simeq 1.9 \times 10^{14} \dot{m}_{\rm CBO,6}^4 A_{\rm in,1}^{-4} M_{\rm CBO,1} \, \text{s},$$

$$t_{\rm mig} = \frac{h_{\rm AGN}^2 M_{\star}^2}{M_{\rm CBO} R_d v_K \Sigma_{\rm AGN}}$$

$$\simeq 1.47 \times 10^{14} \, \alpha_{-1} h_{\rm AGN,-2}^4 M_{\star,8}^{1/2} M_{\rm CBO,1}^{-1} \dot{m}_{\star}^{-1} \, \text{s},$$

$$t_{\rm vis} = \frac{R_d}{\alpha h_{\rm AGN}^2 v_K}$$

$$\simeq 1.39 \times 10^{11} \, \alpha_{-1}^{-1} h_{\rm AGN,-2}^{-2} \mathcal{R}_2^{3/2} M_{\star,8}^{-1/2} \, \text{s}, \tag{5}$$

where $A_{\rm in} \sim 10$ is the ratio of the inner edge of the circumbinary disk surrounding the CBO and the major axis of the binary's orbit (Nixon et al. 2013). We define a critical angle ψ_c above which the condition described by Equation (4) is no longer satisfied and obtain

$$\psi_c \simeq \frac{\pi}{2} - \max[h_{\text{AGN}}, 0.076\mathcal{R}_2^{-1/15} h_{\text{AGN},-2}^{8/15} M_{\star,8}^{1/10}].$$
 (6)

In the equation above, the dependences on the parameters α , η_w , η_{CBO} , and ν_w are not shown, to simplify the notation. Varying $\mathcal R$ in the fiducial range $10{\text -}10^3$, we estimate the critical angle $\psi_c \simeq 85^\circ.6$ and find that ψ_c depends very weakly on $\mathcal R$ and M_\star . This result supports the argument that in most cases a cavity surrounding the CBO is unavoidable and the jet is not choked, except if the binary orbital plane is perpendicular to the AGN disk (Kimura et al. 2021).

2.2. Disk Photon Spectra

The accretion disk can become optically thick to ultraviolet/infrared photons as the plasma gets ionized. We estimate the vertical optical depth, for a fully ionized disk with temperature

 $T_d \gtrsim 10^4 \, \text{K},$

$$\tau_d \approx \Sigma_{\text{AGN}} \kappa_{\text{R}}$$

$$\simeq 7.2 \times 10^3 (1 + X) \dot{m}_{\star} M_{\star,8} \mathcal{R}_2^{-1/2} \alpha_{-1}^{-1} h_{\text{AGN},-2}^{-2}, \tag{7}$$

where $\kappa_R \approx 0.2(1+X)$ is the Rosseland mean opacity for Thomson scattering and X is the hydrogen mass fraction. Since the disk remains optically thick $(\tau_d > 1)$ in the range $\mathcal{R} \sim 10$ – 10^3 , we use a blackbody spectrum to approximate the local photon density (in the units of eV⁻¹ cm⁻³), e.g.,

$$n_{\varepsilon_{\gamma}}^{\text{(eic)}} = \frac{8\pi}{(hc)^3} \frac{\varepsilon_{\gamma}^2}{\exp\left(\frac{\varepsilon_{\gamma}}{k_B T_d}\right) - 1},$$
 (8)

where ε_{γ} is the energy of seed disk photons in the engine frame. The disk temperature T_d at the position of the CBO can be written as (Frank et al. 2002)

$$T_{d} = \left\{ \frac{2GM_{\star}\dot{M}_{\star}}{8\pi\sigma_{S}R_{d}^{3}} \left[1 - \left(\frac{R_{\star}}{R_{d}} \right)^{1/2} \right] \right\}^{1/4}$$

$$\simeq 2.0 \times 10^{4} \, \dot{m}_{\star}^{1/4} M_{\star \, 8}^{-1/4} \mathcal{R}_{2}^{-3/4} \, \text{K}, \tag{9}$$

where $\sigma_{\rm S}$ is the Stefan-Boltzmann constant and R_* is the innermost edge of the disk. In this paper, we consider three distances $\mathcal{R}=10,\ 10^2,\$ and $10^3.$ The corresponding disk temperatures are $k_{\rm B}T_d=9.1,\ 1.7,\$ and $0.3\ {\rm eV}.$ For $R_d\gg R_*,\$ we have $T_d\propto \mathcal{R}^{-3/4},\$ implying that the EIC component becomes increasing important when we move the CBO close to the central SMBH.

3. Nonthermal Electrons

We consider a successful (i.e., nonchoked) GRB jet whose extended emission has a luminosity $L_{j,\rm iso}=10^{48.5}\,{\rm erg\,s^{-1}}.$ We focus on the internal dissipation model in which the jet kinetic energy is dissipated at $R_{\rm dis}=2\Gamma_j^2ct_{\rm var}\simeq 1.5\times 10^{12}\,\Gamma_{j,1.7}^2t_{\rm var,-2}\,{\rm cm}$ via internal shocks (Rees & Meszaros 1994) or magnetic reconnections (McKinney & Uzdensky 2012), where $\Gamma_j=50\Gamma_{j,1.7}$ is the jet Lorentz factor and $t_{\rm var}=10^{-2}t_{\rm var,-2}\,{\rm s}$ is the variability time of velocity fluctuations. One necessary condition for electron acceleration is that the upstream region should be optically thin for the shock not to be radiation mediated, namely, $\tau_{\rm in}=n'\sigma_{\rm T}R_{\rm dis}/\Gamma_j\lesssim 1$ (e.g., Murase & Ioka 2013; Kimura et al. 2018; Yuan et al. 2020), where $n'=L_{j,\rm iso}/(4\pi R_{\rm dis}^2\Gamma_j^2m_pc^3)\simeq 9.6\times 10^{11}\,L_{j,\rm iso,48.5}\Gamma_{j,1.7}^{-6}t_{\rm var}^{-1}\,{\rm cm}^{-3}$ is the comoving number density and $\sigma_{\rm T}$ is the Thomson cross section. Explicitly, we write down the optical depth as $\tau_{\rm in}\simeq 1.8\times 10^{-2}\,L_{j,\rm iso,48.5}\Gamma_{j,1.7}^{-5}t_{\rm var,-2}^{-1}$, which indicates that efficient electron acceleration is plausible.

To get the electron distribution, we numerically solve the steady-state transport equation

$$\frac{\mathcal{N}_{\gamma'_e}}{t_{\rm dyn}'} - \frac{\partial}{\partial \gamma'_e} \left(\frac{\gamma'_e}{t_{e,c}'} \mathcal{N}_{\gamma'_e} \right) = \dot{\mathcal{Q}}'_{e,\rm inj},\tag{10}$$

where γ_e' is the Lorentz factor, $\mathcal{N}_{\gamma_e'} = dN_e/d\gamma_e'$ is the differential spectrum, $t_{\rm dyn}' = R_{\rm dis}/(\Gamma_j c)$ is the dynamical time that may represent adiabatic losses or escape, $t_{e,c}'$ represents the electron cooling timescale, and the function $\dot{Q}_{e,\rm inj}$ is the electron

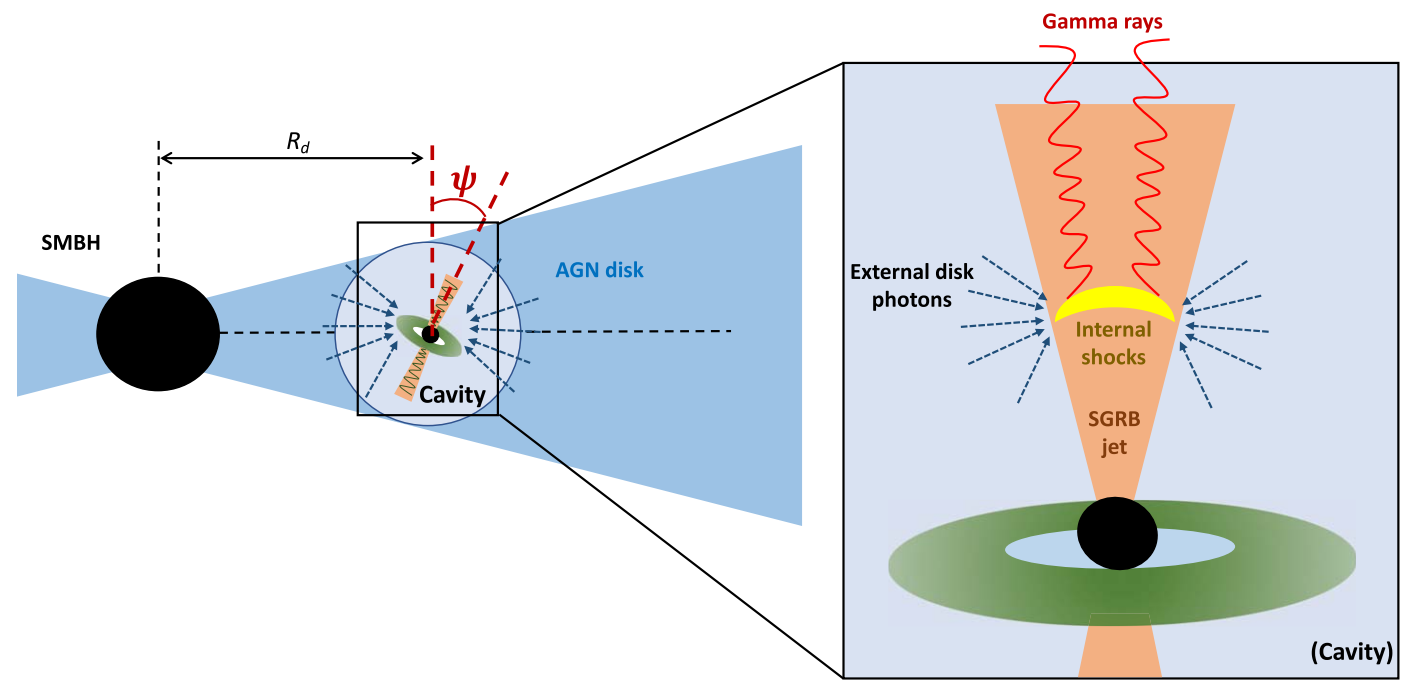


Figure 1. Schematic picture of the CBO mergers embedded in AGN disks. A cavity is formed owing to the powerful outflows from the circumbinary disk. In this configuration, ψ represents the angle between the CBO orbital plane and the AGN disk, and R_d is the distance between the CBO and the central SMBH. Nonthermal electrons accelerated in the internal dissipation region are responsible for the production of γ -rays. These electrons can upscatter the disk photons, leading to the EIC emission

injection rate from shock acceleration. Specifying a spectral index s=2.2, e.g., $\dot{Q}'_{e,\rm inj} \propto \gamma'_e{}^{-s}$, we normalize the injection function via $\int\! d\gamma'_e (\gamma'_e m_e c^2 \dot{Q}'_{e,\rm inj}) = \epsilon_e L_{j,\rm iso} / \Gamma_j^2$. The factor ϵ_e , defined as the fraction of jet kinetic energy that is converted to electrons, is assumed to be $\epsilon_e=0.1$. The minimum Lorentz factor $\gamma'_{e,m}$ for injected electrons is assumed to be $\gamma'_{e,m}=100$.

factor $\gamma'_{e,m}$ for injected electrons is assumed to be $\gamma'_{e,m}=100$. In the dissipation region, the magnetic field is $B'_{\rm dis}=[8\pi\epsilon_B(\Gamma_{\rm rel}-1)n'm_pc^2]^{1/2}\simeq 3.8\times 10^4~\epsilon_{B,-2}^{1/2}L_{\rm j,iso,48.5}^{1/2}\Gamma_{\rm j,i.7}^{-3}t_{\rm var}^{-1/2}~{\rm G}$, where $\Gamma_{\rm rel}\simeq 5$ is the relative Lorentz factor between the fast and slow shells. The ratio of $B'_{\rm dis}$ to the disk magnetic field B_d is $B_{\rm dis}{}'/(\Gamma_j B_d)\simeq 3.8~\mathcal{R}_2^{9/8}\beta_{0.48}^{1/2}$. Here we focus on the \mathcal{R} -dependence of the magnetic fields, using the fiducial values for all other parameters. We use the modulated magnetic field $B'=\max[B_{\rm dis}{}',\Gamma_j B_d]$ to calculate the electromagnetic emission in the dissipation region.

The accelerated electrons lose energy through synchrotron, SSC, and EIC processes within the corresponding timescales $t_{e,\rm syn}', t_{e,\rm ssc}',$ and $t_{e,\rm eic}'$. The net cooling timescale is given by $t_{e,c}' = (t'_{e,\rm syn}^{-1} + t'_{e,\rm esc}^{-1} + t'_{e,\rm eic}^{-1})^{-1}$. Electrons with higher γ_e' cool down faster, while a longer acceleration time, e.g., $t'_{\rm acc} = \gamma_e' m_e c/(eB')$, is required to reach such a high energy. We thus expect a cutoff Lorentz factor $\gamma_{e,\rm cut}'$ determined by the equation $t'_{\rm acc} = t'_{e,c}$, above which electrons cannot accumulate energy owing to the rapid radiation. Using these arguments, the injection function for a spectral index s > 2.0 can be written as

$$\dot{Q}'_{e,\text{inj}} = \frac{(s-2)\,\epsilon_e L_{j,\text{iso}}}{\Gamma_j^2 m_e c^2 \gamma'_{e,m}^2} \left(\frac{\gamma'_e}{\gamma'_{e,m}}\right)^{-s} \exp\left(-\frac{\gamma'_e}{\gamma'_{e,\text{cut}}}\right). \tag{11}$$

The photons from the synchrotron process play the role of seed photons in EIC scattering. Therefore, we need a trial electron spectrum, e.g., $\mathcal{N}_{\gamma'_e}^{(0)} \sim (t'_{\rm dyn}^{-1} + t'_{e,\rm syn}^{-1} + t'_{e,\rm eic}^{-1})^{-1} \dot{Q}'_{e,\rm inj}$, to

evaluate $t'_{\rm ssc}$ and solve the differential Equation (10) iteratively to obtain a convergent solution as in Zhang et al. (2021a).

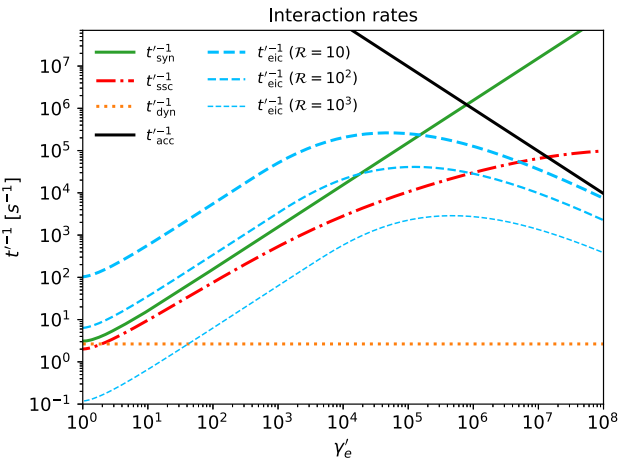
The left panel of Figure 2 shows the energy-loss rates. The blue dashed lines show the EIC cooling rate for $\mathcal{R} = 10, 10^2$, and 10³. The synchrotron (green line) and SSC (red dasheddotted line) cooling rates are not sensitive to the CBO's position, whereas the EIC rate increases as the distance between the CBO and the SMBH reduces. This tendency is consistent with Equation (9), which predicts a hotter and photon-denser environment close to the SMBH. Remarkably, the EIC process starts to dominate the electron cooling at a distance range $\mathcal{R} \lesssim 10^2$, leading to a softer electron spectrum, e.g., the blue line ($\mathcal{R}=10$) in the right panel of Figure 2, in contrast to the high- \mathcal{R} cases. The black solid line in the right panel shows the electron injection function. In the low-energy band, there is no injection, e.g., $\dot{Q}_{e,\rm inj}=0$ for $\gamma_e'\lesssim\gamma_{e,m}'$, and we can analytically solve Equation (10) and connect this segment to the $\gamma_e'>\gamma_{e,m}'$ part. Using the simplification $t_c^{\prime -1} \sim b \gamma_c^{\prime}$, which is consistent with the EIC and synchrotron cooling rates in the left panel, we obtain

$$\mathcal{N}_{\gamma'_{e}} = \mathcal{N}_{\gamma'_{e,m}} \exp\left[-\frac{1}{bt'_{\text{dyn}}}(\gamma'_{e,m} - \gamma'_{e})\right], \ \gamma'_{e} \lesssim \gamma'_{e,m}, \quad (12)$$

where $\mathcal{N}_{\gamma'_{e,m}}$ represents the electron number distribution at $\gamma'_{e,m}$. Equation (12) explains the electron spectrum softening at lower values of \mathcal{R} (equivalently at larger values of b).

4. Results

Using the electron spectra obtained in Section 3 and following the formalism and procedures presented in Murase



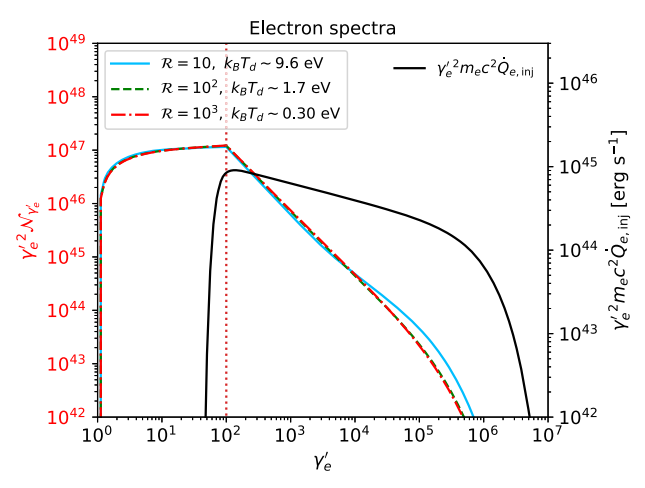


Figure 2. Left panel: energy-loss rates of accelerated electrons in the internal dissipation region. The green solid and red dashed–dotted lines show the synchrotron and SSC rates, respectively. From thick to thin, the blue dashed lines depict the EIC cooling rate for the CBOs at $\mathcal{R}=10$, 10^2 , and 10^3 , respectively. The reciprocals of the dynamic and acceleration times are illustrated as the yellow dotted and black solid lines, respectively. Right panel: the electron number spectra as functions of the electron Lorentz factor. The minimum injected Lorentz factor is $\gamma'_{e,m}=100$. The blue solid, green dashed, and red dashed–dotted lines correspond to $\mathcal{R}=10$, 10^2 , and 10^3 cases, respectively. The black solid line is the electron injection function.

et al. (2011), Zhang et al. (2021a), and Yuan et al. (2021), we numerically compute the γ -ray spectra taking into account the synchrotron, SSC, and EIC processes. We consider three merger-induced GRBs in an AGN located at redshift z=1 (the equivalent luminosity distance is $d_L \simeq 6.7$ Gpc). We focus on the on-axis case and assume that the CBOs' orbit planes are all aligned with the AGN disk plane, e.g., $\psi = 0$. A discussion on the influence of ψ will be given in Section 4.2.

While propagating in the jet and in the AGN disk, highenergy γ -rays will annihilate with ambient UV/IR disk photons, resulting in their attenuation and EM cascades. The optical depth for $\gamma\gamma$ annihilation depends on the photon energy in the short GRB's engine frame $\varepsilon_{\gamma} = \Gamma_{j}\varepsilon_{\gamma}'$, the position of the jet, and the misalignment angle ψ , via

$$\tau_{\gamma\gamma}[\varepsilon_{\gamma}, \mathcal{R}, \psi] \approx \int_{0}^{H_{AGN}} \frac{dy}{\cos \psi} \lambda_{\gamma\gamma}^{-1}[\varepsilon_{\gamma}, R_d + y \tan \psi], \quad (13)$$

where the reciprocal of the mean free path $\lambda_{\gamma\gamma}[R_d]$ for an isotropic disk photon field can be calculated as (e.g., Dermer & Menon 2009)

$$\lambda_{\gamma\gamma}^{-1}[\varepsilon_{\gamma}, R_d] = \frac{1}{2} \int_{-1}^{1} d\mu (1 - \mu) \int d\tilde{\varepsilon}_{\gamma} n_{\epsilon_{\gamma}}^{(\text{eic})}[\tilde{\varepsilon}_{\gamma}] \sigma_{\gamma\gamma}[x]. \tag{14}$$

In this expression, $x = \tilde{\varepsilon}_{\gamma} \varepsilon_{\gamma} (1 - \mu)/2$ is the particle Lorentz factor in the center-of-momentum frame and $\sigma_{\gamma\gamma}$ is the $\gamma\gamma$ annihilation cross section.

Figure 3 shows the optical depth in the observer's frame, where the observed energy is connected with ε_{γ} and ε_{γ}' via $E_{\gamma} = \varepsilon_{\gamma}/(1+z) = \Gamma_{j}\varepsilon_{\gamma}'/(1+z)$. The solid blue, yellow, and red lines illustrate $\tau_{\gamma\gamma}$ at $\mathcal{R}=10,\ 10^{2},\$ and $10^{3},\$ respectively, with $\psi=0$, whereas the dashed lines correspond to the case of an inclined jet, e.g., $\psi=45^{\circ}$. The universe becomes opaque for γ -rays produced at z=1 with energies $E_{\gamma}\gtrsim 220\$ GeV (see the gray area in Figure 3) owing to $\gamma\gamma$ annihilation between γ -rays and cosmic backgrounds (Finke et al. 2010), e.g., extragalactic background light (EBL) and cosmic microwave background (CMB). From Figure 3, we find that γ -rays with energy $E_{\gamma}\gtrsim 10\$ GeV are strongly suppressed owing to $\gamma\gamma$ annihilation for a GRB close to the SMBH, i.e., $\mathcal{R}\simeq 10$. For a GRB at

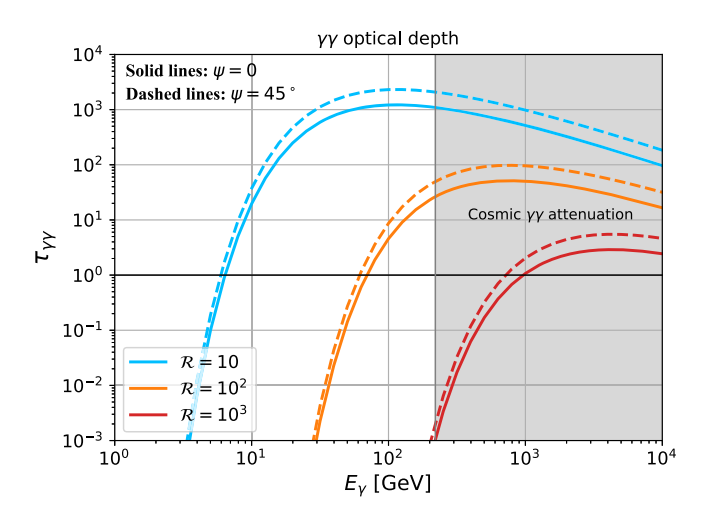


Figure 3. The blue ($\mathcal{R}=10$), yellow ($\mathcal{R}=10^2$), and red ($\mathcal{R}=10^3$) lines are the optical depth $\tau_{\gamma\gamma}$ for $\gamma\gamma$ annihilation between γ -rays and disk photons. The solid and dashed lines correspond to the inclination $\psi=0$ and $\psi=45^\circ$. The optical depth to cosmic $\gamma\gamma$ annihilation becomes greater than 1.0 in the energy range $E_{\gamma}\gtrsim 220$ GeV (the gray shaded area), assuming that the CBO merger is located at z=1.0.

positions with a larger $\mathcal{R} \sim 10^2 - 10^3$, γ -ray photons with energy $E_{\gamma} \sim 100 \, \text{GeV}$ can escape from the AGN disk.

Applying the factor $\exp(-\tau_{\gamma\gamma})$ to the γ -ray spectra, we obtain the $\gamma\gamma$ -attenuated spectra for embedded GRBs at redshift z=1, as shown in Figure 4. In this figure, $\psi=0$ is used. The blue solid, yellow solid, and red dashed lines illustrate the synchrotron, SSC, and EIC components, respectively. The dotted lines with corresponding colors show the fluxes before $\gamma\gamma$ attenuation. The gray dashed–dotted lines indicate the CTA flux sensitivity for the 10^3 s observation time (Al Samarai et al. 2019). The magenta dashed lines show the disk photon fluxes multiplied by 10^4 . From the red dashed lines in Figure 4, we find that a closely embedded GRB can produce brighter γ -ray emission owing to the EIC enhancement. The "Compton dominance" induced by EIC enhancement can be used as the prominent feature to distinguish these embedded short GRBs from others.

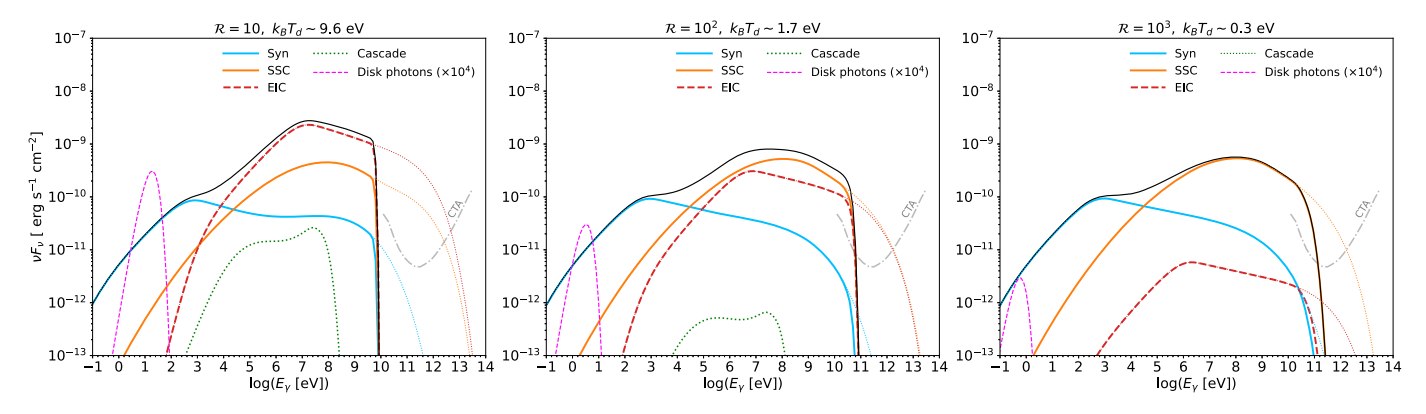


Figure 4. The observed γ -ray spectra from embedded short GRBs at z=1 with distances $\mathcal{R}=10$ (left panel), 10^2 (middle panel), and 10^3 (right panel) to the central SMBH. The GRB parameters used here are the fiducial parameters assumed in Section 3, e.g., $L_{j,iso}=10^{48.5}$ erg s⁻¹, $\Gamma_j=50$, $\epsilon_B=0.01$, and $\epsilon_e=0.1$. The blue, yellow, and red solid lines show the synchrotron, SSC, and EIC emission after $\gamma\gamma$ attenuation, respectively. The dotted lines in the corresponding colors depict the unattenuated fluxes. The cascade emissions are depicted as the green lines. The magenta dashed lines show the disk target photon fluxes (multiplied by 10^4). In both cases, $\psi=0$ is applied. The gray dashed–dotted lines indicate the CTA flux sensitivity for the 10^3 s observation time.

The e^+/e^- pairs produced in the $\gamma\gamma$ annihilation process will induce electromagnetic cascades while diffusing and cooling down in the AGN disk via synchrotron and inverse Compton processes. Following the treatment in Murase et al. (2007), we write down the distribution for the secondary electrons and positrons,

$$\mathcal{N}_{\gamma_e}^{\rm cas} \approx 2\mathcal{N}_{\hat{\varepsilon}_{\gamma}}^{\rm ph} \left(\frac{d\hat{\varepsilon}_{\gamma}}{d\gamma_e} \right) (1 - e^{-\tau_{\gamma\gamma}[\hat{\varepsilon}_{\gamma}, \mathcal{R}, \psi]}),$$
 (15)

where $N_{\hat{\epsilon}_{\alpha}}^{\text{ph}}$ is the pre-attenuation gamma-ray number spectra (in the units of eV^{-1}) in the engine frame and $\hat{\varepsilon}_{\gamma} = 2\gamma_e m_e c^2$ is the energy of primary electrons. Using the cavity magnetic field $B_{\rm cav} \approx (2\epsilon_B \eta_w \dot{M}_{\rm CBO} v_w / H_{\rm AGN}^2)^{1/2} \simeq$ 98 $\epsilon_{B,-2}^{1/2} \eta_{w,-0.5}^{1/2} h_{\text{AGN},-2}^{-1} \eta_{\text{CBO},-1}^{1/2} \mathcal{R}_{2}^{-1} \dot{m}_{\star}^{1/2} M_{\star,8}^{-1/2} v_{w,9}^{1/2} \text{ G},$ numerically calculate the cascade emission. The green dotted lines in Figure 4 show the cascade emission. Comparing to the beamed emission produced in the jet, the cascade emission is subdominant for $\mathcal{R}\gtrsim 100$ and typically peaks at a lower energy $\sim 100 \, \text{MeV}$. We find that the cascade flux drops dramatically as \mathcal{R} increases, which is consistent with the \mathcal{R} -dependence of the $\gamma\gamma$ optical depth in Figure 3. When the disk becomes transparent to the γ -ray photons, the e^-/e^+ pair production is suspended and the cascade emission is strongly suppressed. Typically, we need to solve the timedependent equations to obtain the secondary electron/ position distributions and the cascade spectrum. Our approach can provide a good estimation since these secondary particles cool down very fast, e.g., $t_{e,c}^{\text{cas}} \lesssim 10 \text{ s.}$

4.2. Detectability with Fermi-LAT and VHE γ -Ray Facilities

It is useful to compare the expected γ -ray fluxes in the extended emission phase against the sensitivities of current and future facilities, such as Fermi-LAT, MAGIC, H.E.S.S., VERITAS, CTA, and LHAASO-WCDA, and discuss how the parameters $\mathcal R$ and ψ influence the results.

Observationally, a significant fraction of short GRBs exhibit "long-lasting" extended or plateau emission peaking in X-ray bands (Norris & Bonnell 2006; Sakamoto et al. 2011; Kaneko et al. 2015; Kisaka et al. 2017) with the duration $T_{\rm dur} \sim 10^2 - 10^5$ s, following the prompt phase where 90% of

the kinetic energy is dissipated in \sim 2 s, e.g., $T_{90} \lesssim$ 2 s. Such prolonged emission may originate from the continuous energy injection by the accreting BHs formed after the merger or the fast-rotating magnetars (e.g., Dai et al. 2006; Metzger et al. 2008; Barkov & Pozanenko 2011; Bucciantini et al. 2012; Rowlinson et al. 2013; Gompertz et al. 2014; Kisaka & Ioka 2015). Considering a prolonged γ -ray emission of luminosity $L_{j,\rm iso} = 10^{48.5} \, {\rm erg \, s^{-1}}$ and the corresponding duration in the observer's frame $T_{\rm dur} \sim 10^2 - 10^3 \, {\rm s}$, we show the integral sensitivities within $T_{\rm dur}$ for Fermi-LAT⁶ and CTA (Al Samarai et al. 2019) at $E_{\gamma} = 1$ GeV (yellow area), 25 GeV (blue area), and 100 GeV (red area) in the left panel of Figure 5. The upper and lower bounds of each shaded area demonstrate the performances for the detectors given the observation times $T_{\rm dur} = 10^2$ and 10^3 s, respectively. We plot also the 1 GeV (yellow lines), 25 GeV (blue lines), and 100 GeV (red lines) fluxes as functions of \mathcal{R} in the left panel of Figure 5. The solid lines correspond to the $\psi = 0$ case, whereas the dashed and dashed-dotted lines depict the $\psi = 45^{\circ}$ and $\psi = 75^{\circ}$ cases. The thick lines are for the GRBs at z = 1, while the thin yellow line shows the 1 GeV fluxes for a closer GRB at z = 0.1 $(d_L \simeq 460 \,\mathrm{Mpc}).$

The influence of disk photons is encoded in the shapes of the yellow, blue, and red curves. The 1 GeV flux decreases to a flat level as $\mathcal R$ increases because the EIC component gradually becomes less important as the CBO is moved to a cooler outer region. In the ranges $\mathcal R\lesssim 50$ and $\mathcal R\lesssim 300$, the $\gamma\gamma$ attenuation caused by dense disk photons suppresses the 25 and 100 GeV emission, respectively. Since the $\gamma\gamma$ annihilation is negligible for 1 GeV photons even if the CBO is very close to the SMBH (see the blue lines in Figure 3), we expect that the flux does not depend on ψ . On the other hand, the 25 and 100 GeV fluxes decrease as ψ approaches $\psi_c \simeq 85^\circ.6$.

From the left panel of Figure 5, we find that CTA will be capable of detecting 25 and 100 GeV γ -rays up to z=1 if an embedded short GRB is appropriately distant from the SMBH, e.g., $\mathcal{R} \gtrsim 40$ for 25 GeV γ -rays and $\mathcal{R} \gtrsim 200$ for 100 GeV γ -rays. By contrast, it is challenging for Fermi-LAT to detect the 1 GeV photons from sources located at z=1 via point-source search within the duration $T_{\rm dur} \sim 10^3$ s. For the short GRBs

⁶ The Fermi-LAT sensitivity can be found in https://www.slac.stanford.edu/exp/glast/groups/canda/lat_Performance.htm.

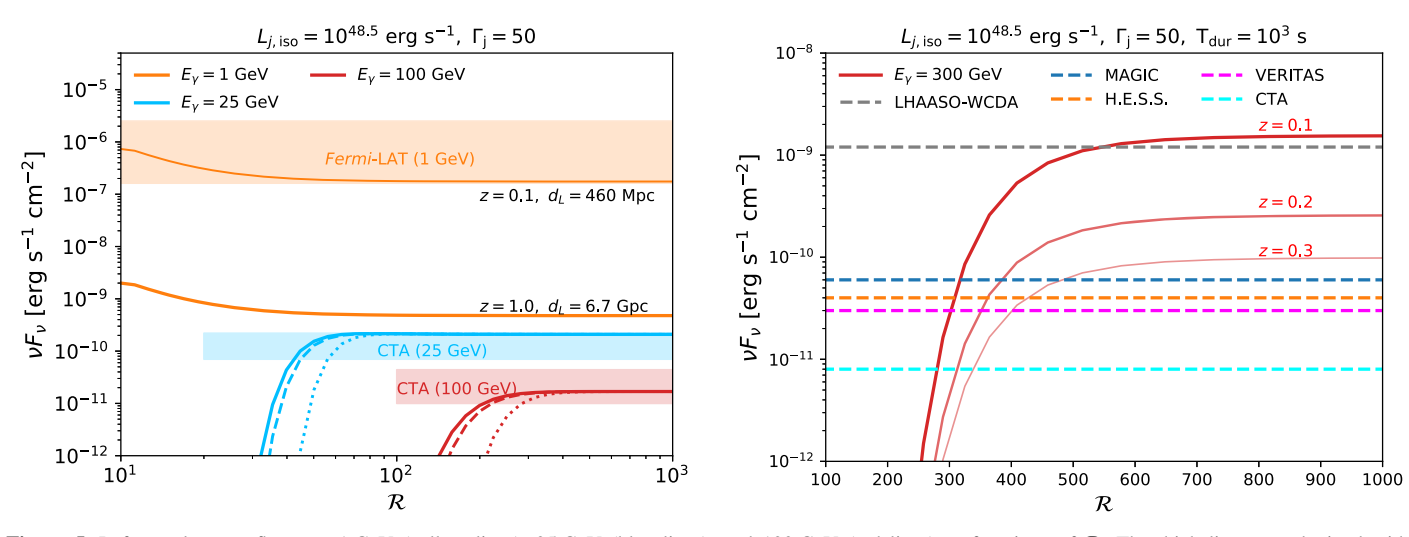


Figure 5. Left panel: γ -ray fluxes at 1 GeV (yellow lines), 25 GeV (blue lines), and 100 GeV (red lines) as functions of \mathcal{R} . The thick lines are obtained with $L_{j,\mathrm{iso}} = 10^{48.5}$ erg s⁻¹ and z = 1.0, whereas a closer short GRB at z = 0.1 is considered for the thin yellow line. The point-source performances for Fermi-LAT and CTA at corresponding energies are shown as the yellow, blue, and red areas, respectively. The upper and lower bounds show the sensitivities for the observation time $T_{\mathrm{dur}} = 10^2$ and 10^3 s. Right panel: the red solid lines from thick to thin show the \mathcal{R} -dependence of 300 GeV γ -ray fluxes from the embedded short GRBs at z = 0.1, 0.2, and 0.3. The horizontal dashed lines from top to bottom correspond to the sensitivities of LHAASO-WCDA, MAGIC, H.E.S.S., VERITAS, and CTA.

embedded in AGN disks, we would require a nearby CBO merger ($d_L \lesssim 460 \, \mathrm{Mpc}$) at the position with the distance greater than $40 R_{\mathrm{S}}$ ($\mathcal{R} \gtrsim 40$) to the central SMBH in order to be detected simultaneously by CTA and Fermi-LAT.

MAGIC, H.E.S.S., and VERITAS are current ground Imaging Atmospheric Cherenkov Telescopes with very good performance in the energy range 150 GeV-30 TeV. LHAASO a new-generation multicomponent instrument, and LHAASO-WCDA is operated in the energy range \sim 300 GeV -10 TeV. We present the \mathcal{R} -dependence of 300 GeV γ -ray fluxes at z = 0.1, 0.2, and 0.3 (the red solid lines, from thick to thin) in the right panel of Figure 5. The horizontal dashed lines from top to bottom correspond to the flux sensitivities of LHAASO-WCDA (Bai et al. 2019), MAGIC (Aleksić et al. 2016), H.E.S.S. (Holler et al. 2015), VERITAS, and CTA for $T_{\rm dur}=10^3\,{\rm s}$ and $\psi=0$. At 300 GeV, the sensitivity of LHAASO-WCDA is $\sim\!10^{-9}\,{\rm erg\,s^{-1}\,cm^{-2}}$ in $10^3\,{\rm s}$ observation. The nearby embedded GRBs with redshift z < 0.1 can be observed. MAGIC, H.E.S.S., VERITAS, and CTA can detect 300 GeV photons from embedded GRBs up to redshift z = 0.3if $\mathcal{R} \gtrsim 500$ is satisfied. For the sources with farther distance, the universe could be opaque to VHE γ -rays.

4.3. Prompt Emission

As for the prompt emission, besides the cutoff with energy $\gtrsim 100~{\rm GeV}$ caused by the $\gamma\gamma$ absorption in the AGN disk, we found that there may be no significant difference between short GRBs embedded in AGN disks and other short GRBs. The reason is that, given a higher isotropic luminosity $L_{j,\rm iso}^{\rm prompt} = 10^{51}~{\rm erg~s^{-1}}$ and a higher Lorentz factor $\Gamma_j^{\rm prompt} = 200~(\Gamma_j^{\rm prompt} = 100)$ in the prompt emission phase of $T_{90} = 1~{\rm s}$, the EIC emission is subdominant (comparable) compared to the synchrotron/SSC components. Using the parameters in the prompt emission phase, we estimate photon

flux in the energy range 50-300 keV,

$$F_{\nu,50-300 \text{ keV}}^{\text{prompt}} \simeq 1.9 (1+z) d_{L,28}^{-2} \text{ ph s}^{-1} \text{ cm}^{-2}.$$
 (16)

Noting that the onboard trigger threshold of the Fermi Gamma-Ray Burst Monitor (Fermi-GBM) is ~ 0.7 photons s⁻¹ cm⁻² (Meegan et al. 2009), it can detect the prompt emission and localize the short GRB. At 10 GeV, the flux of the prompt emission is $\nu F_{\nu,10\,\mathrm{GeV}}^{\mathrm{prompt}} \sim 2 \times 10^{-6} \, (1+z) d_{L,28}^{-2} \, \mathrm{erg \, s^{-1} \, cm^{-2}}$, implying the possible detection of the embedded GRBs at $z \sim 0.5$ –1 with the High Altitude Water Cherenkov (HAWC) observatory (Abeysekara et al. 2012). If the short GRB is GRB 090510–like, e.g., $L_{j,\mathrm{iso}}^{\mathrm{prompt}} \gtrsim 10^{53} \, \mathrm{erg \, s^{-1}}$, Fermi-LAT would also be able to see γ -ray photons up to $\sim 30 \, \mathrm{GeV}$ in the prompt emission phase (Ackermann et al. 2010). Above all, the prompt emission diagnosis can provide valuable information for the follow-up observations of extended emissions.

5. Summary and Discussion

We studied γ -ray emission from short GRBs embedded in AGN disks and showed that successful jets are expected from these, since the CBOs in the disks are highly super-Eddington accretors and can produce low-density cavities around the CBO via powerful outflows. Our work demonstrates that the AGN disks influence the γ -ray emission mainly in two ways, namely, via the EIC enhancement and $\gamma\gamma$ attenuation, depending on the distance to the SMBH and the inclination ψ . If a CBO merger occurs very close to the SMBH, e.g., $\mathcal{R}\sim 10$ -40, the dense disk photon field will lead to a luminous EIC component in the GeV band and a firm cutoff at $E_{\gamma} \simeq 10$ GeV. On the other hand, the SSC process dominates the GeV emission for CBO mergers at $\mathcal{R} \gtrsim 100$, and the disk gradually becomes transparent for 10-100 GeV photons unless the GRB jet is entirely buried inside the AGN disk, e.g., $\psi \gtrsim \psi_c \simeq 85^\circ$ 6. Considering the ratio of the peak flux of the inverse Compton component to the synchrotron peak flux and the cutoff energy, we may be able to distinguish the short GRBs embedded in AGN disks from other types of isolated short GRBs (e.g., Murase et al. 2018; Kimura et al. 2019). To identify the embedded short GRBs, we can

⁷ The differential sensitivity of VERITAS can be found in https://veritas.sao. arizona.edu/about-veritas/veritas-specifications.

utilize these two signatures, "Compton dominance" and $\gamma\gamma$ annihilation cutoff. Such spectral information can also be used to determine the parameters of the short GRB-AGN disk system such as T_d , \mathcal{R} , and ψ . According to the simulations of compact binary formations in AGN disks, it is reasonable to expect the embedded short GRBs to occur in the region $\mathcal{R}\gtrsim 40$ –100 (Bellovary et al. 2016; Tagawa et al. 2020). The detection of these short GRBs can, in return, be used to test current AGN-assisted CBO formation theories and constrain the CBO distributions in AGN disks.

Since approximately $f_{\rm EE} \sim 1/4 - 1/2$ (e.g., Bucciantini et al. 2012) of Swift short GRBs are accompanied by extended emission, we investigated the detectability of GRBs in the AGN disk for CTA and Fermi-LAT considering a jet of luminosity $L_{j,\rm iso}=10^{48.5}\,{\rm erg\,s^{-1}}$ lasting for $T_{\rm dur}\sim10^2-10^3\,{\rm s}$. From now on, we discuss the detection perspectives of the extended emissions with $T_{\rm dur}=10^2-10^3\,{\rm s}$, $L_{\rm j,iso}=10^{48.5}\,{\rm erg\,s^{-1}\,cm^{-2}}$, and $\Gamma_j=50$. For the embedded short GRBs within z = 1.0, CTA will be able to detect the γ -rays in the energy range $E_{\gamma} \sim 25-100 \, \text{GeV}$ if the requirements $\mathcal{R} \gtrsim \mathcal{R}_c$ and $\psi \lesssim \psi_c$ are satisfied, where $\mathcal{R}_c \sim 40$ –100 is the critical distance defined by $\tau_{\gamma\gamma}[(1+z)E_{\gamma}, \mathcal{R}_{c}, \psi] = 1$. To estimate the CTA detection rate, we use $f_{\mathcal{R}}$ and $f_{\psi}\!\sim\!1$ to represent the fractions of embedded short GRBs that meet the conditions $\mathcal{R} \gtrsim \mathcal{R}_c$ and $\psi \lesssim \psi_c$, respectively. Taking into account both NS-NS and NS-BH mergers, McKernan et al. (2020) estimated the occurrence rate of short GRBs in AGN disks at z < 1, $\dot{R}_{SGRB,AGN} \sim (300 - 2 \times 10^4) f_{AGN,-1} \text{ yr}^{-1}$, where $f_{\rm AGN} \sim 0.1$ is the fraction of BH-BH mergers. We estimate the CTA detection rate of the on-axis prolonged γ -ray emission from short GRBs embedded in AGN disks via $\dot{R}_{\text{CTA}} \sim f_{\text{CTA}} f_b f_{\text{EE}} f_{\mathcal{R}} f_{\psi} \dot{R}_{\text{GRB,AGN}} \sim (0.2\text{-}22) f_{\mathcal{R}} \theta_{j,-1}^2 f_{\text{AGN},-1} \text{ yr}^{-1}$, where $f_{\text{CTA}} \sim 0.3\text{-}0.5$ is the CTA detection efficiency defined as the ratio of detectable events to events that can be followed up by CTA (e.g., Inoue et al. 2013), $f_b = (\theta_j + 1/\Gamma_j)^2/2 \sim \theta_j^2/2$ is the beaming factor, and $\theta_j \sim 0.1$ is the jet opening angle. Despite the large uncertainty in the CTA detection rate, we estimate that it is feasible for CTA to detect the prolonged γ -ray emission from short GRBs embedded in AGN disks in the timescale of 1 yr.

We now discuss the implications for multimessenger analyses with GWs and γ -rays. Bartos et al. (2017) estimated that the merger rate of BBHs embedded in AGN disks within the advanced Laser Interferometer Gravitational-wave Observatory's (aLIGO's) horizon, e.g., $D_h \simeq 450\,\mathrm{Mpc}$, could be $\dot{R}_{\mathrm{L,BBH}} \sim 20\,\mathrm{yr}^{-1}$. Implementing the ratio of the cumulative NS-BH and NS-NS merger rates to the BBH merger rate in the AGN channel, $f_{\mathrm{L,CBO/BBH}} = (\dot{R}_{\mathrm{L,NS-NS}} + \dot{R}_{\mathrm{L,NS-BH}})/\dot{R}_{\mathrm{L,BBH}} \sim 0.1$ –7.0 (McKernan et al. 2020), we estimate the occurrence rate of on-axis short GRBs with extended emission originating from LIGO-detectable CBO mergers in the AGN channel,

$$\dot{R}_{\rm SGRB-AGN}^{(L)} = f_{\rm EE} f_b f_{\rm L,CBO/BBH} \dot{R}_{\rm L,BBH} \sim (2.5 \times 10^{-3} - 0.35) \,\theta_{j,-1}^2 \,\rm yr^{-1}. \tag{17}$$

The physical meaning of this equation is that among all detectable mergers within LIGO's horizon, MAGIC, H.E.S.S., VERITAS, CTA, and LHAASO-WCDA can observe 2.5×10^{-3} –0.35 short GRBs with extended γ -ray emission each year. In the optimistic case, it is possible to detect the

on-axis extended emission simultaneously with GWs originating from CBO mergers embedded in AGN disks in one decade.

We note also that, while this is not the subject of the present work, the model predicts that short GRBs from CBO mergers are efficient neutrino emitters. Our model does not require choked jets, unlike Zhu et al. (2021b, 2021c). The cosmic rays accelerated in the successful jet can efficiently interact with disk photons and produce high-energy neutrinos via the photomeson production process. Using Equations (8) and (9) of Murase et al. (2016) and Figure 3 of this work, the photomeson optical depth is $f_{p\gamma} \sim 1$ for $\mathcal{R} \sim 10$ and $f_{p\gamma} \sim 0.1$ for $\mathcal{R} \sim 100$. High-energy neutrinos are expected in the PeV range, and they will make an additional contribution to those predicted by Kimura et al. (2017). The enhancement is more prominent for prompt neutrino emission because the efficiency is low for usual short GRBs.

In conclusion, future multimessenger analyses of AGN short GRBs can provide unprecedented insights for understanding the formation and evolution of CBOs inside the AGN disks, as well as on the origin of their high-energy emission.

We thank B. Theodore Zhang, Mukul Bhattacharya, Zsuzsa Márka, and Szabolcs Márka for fruitful discussions. C.C.Y. and P.M. acknowledge support from the Eberly Foundation. The work of K.M. is supported by NSF grant Nos. AST-1908689, AST-2108466, and AST-2108467 and KAKENHI grant Nos. 20H01901 and 20H05852. A.P. is supported by the European Research Council via ERC consolidating grant 773062 (acronym O.M.J.). I.B. acknowledges the support of NSF under awards PHY-1911796 and PHY-2110060 and the Alfred P. Sloan Foundation.

ORCID iDs

Chengchao Yuan https://orcid.org/0000-0003-0327-6136 Kohta Murase https://orcid.org/0000-0002-5358-5642 Asaf Pe'er https://orcid.org/0000-0001-8667-0889 Péter Mészáros https://orcid.org/0000-0002-4132-1746

References

```
Abbott, B. P., Abbott, R., Abbott, T. D., et al. 2017a, ApJL, 848, L12
Abbott, B. P., Abbott, R., Abbott, T. D., et al. 2017b, ApJ, 848, L13
Abbott, B. P., Abbott, R., Abbott, T. D., et al. 2017c, Natur, 551, 85
Abbott, B. P., Abbott, R., Abbott, T. D., et al. 2017d, PhRvL, 119, 161101
Abeysekara, A. U., Aguilar, J. A., Aguilar, S., et al. 2012, APh, 35, 641
Ackermann, M., Asano, K., Atwood, W. B., et al. 2010, ApJ, 716, 1178
Al Samarai, I., Batista, R. A., de Almeida, U. B., et al. 2019, Science with the
   Cherenkov Telescope Array (Singapore: World Scientific)
Aleksić, J., Ansoldi, S., Antonelli, L. A., et al. 2016, APh, 72, 76
Ashton, G., Ackley, K., Hernandez, I. M., & Piotrzkowski, B. 2021, CQGra,
  38, 235004
Bai, X., Bi, B. Y., Bi, X. J., et al. 2019, arXiv:1905.02773
Barkov, M. V., & Pozanenko, A. S. 2011, MNRAS, 417, 2161
Bartos, I. 2021, AAS Meeting Abstracts, 53, 234.02
Bartos, I., Kocsis, B., Haiman, Z., & Márka, S. 2017, ApJ, 835, 165
Bellovary, J. M., Mac Low, M.-M., McKernan, B., & Ford, K. E. S. 2016,
  ApJL, 819, L17
Berger, E. 2014, ARA&A, 52, 43
Bucciantini, N., Metzger, B. D., Thompson, T. A., & Quataert, E. 2012,
    MNRAS, 419, 1537
Dai, Z. G., Wang, X. Y., Wu, X. F., & Zhang, B. 2006, Sci, 311, 1127
Dermer, C. D., & Menon, G. 2009, High Energy Radiation from Black Holes:
  Gamma Rays, Cosmic Rays, and Neutrinos (Princeton: Princeton Univ.
```

Eichler, D., Livio, M., Piran, T., & Schramm, D. N. 1989, Natur, 340, 126

Finke, J. D., Razzaque, S., & Dermer, C. D. 2010, ApJ, 712, 238

```
Frank, J., King, A., & Raine, D. J. 2002, Accretion Power in Astrophysics:
   Third Edition (Cambridge: Cambridge Univ. Press)
Gayathri, V., Bartos, I., Haiman, Z., et al. 2020, ApJL, 890, L20
Goldstein, A., Veres, P., Burns, E., et al. 2017, ApJL, 848, L14
Gompertz, B. P., O'Brien, P. T., & Wynn, G. A. 2014, MNRAS, 438, 240
Gottlieb, O., Levinson, A., & Nakar, E. 2019, MNRAS, 488, 1416
Graham, M. J., Ford, K. E. S., McKernan, B., et al. 2020, PhRvL, 124, 251102
Hallinan, G., Corsi, A., Mooley, K. P., et al. 2017, Sci, 358, 1579
Hjorth, J., & Bloom, J. S. 2012, in The GRB-supernova Connection,
   Cambridge Astrophysics, ed. C. Kouveliotou, R. A. M. J. Wijers, &
   S. Woosley (Cambridge: Cambridge Univ. Press), 169
Holler, M., Berge, D., van Eldik, C., et al. 2015, arXiv:1509.02902
Inoue, S., Granot, J., O'Brien, P. T., et al. 2013, APh, 43, 252
Ioka, K., & Nakamura, T. 2019, MNRAS, 487, 4884
Jiang, Y.-F., Stone, J. M., & Davis, S. W. 2014, ApJ, 796, 106
Jiao, C.-L., Mineshige, S., Takeuchi, S., & Ohsuga, K. 2015, ApJ, 806, 93
Kanagawa, K. D., Tanaka, H., Muto, T., Tanigawa, T., & Takeuchi, T. 2015,
          S. 448, 994
Kaneko, Y., Bostancı, Z. F., Göğüş, E., & Lin, L. 2015, MNRAS, 452, 824
Kimura, S. S., Murase, K., Bartos, I., et al. 2018, PhRvD, 98, 043020
Kimura, S. S., Murase, K., & Bartos, I. 2021, ApJ, 916, 111
Kimura, S. S., Murase, K., Ioka, K., et al. 2019, ApJL, 887, L16
Kimura, S. S., Murase, K., Mészáros, P., & Kiuchi, K. 2017, ApJL, 848, L4
Kisaka, S., & Ioka, K. 2015, ApJL, 804, L16
Kisaka, S., Ioka, K., & Sakamoto, T. 2017, ApJ, 846, 142
Kitaki, T., Mineshige, S., Ohsuga, K., & Kawashima, T. 2018, PASJ, 70, 108
Koo, B.-C., & McKee, C. F. 1992, ApJ, 388, 93
Lazzati, D., Perna, R., Morsony, B. J., et al. 2018, PhRvL, 120, 241103
Lee, W. H., & Ramirez-Ruiz, E. 2007, NJPh, 9, 17
Lyman, J. D., Lamb, G. P., Levan, A. J., et al. 2018, NatAs, 2, 751
MacFadyen, A. I., & Woosley, S. E. 1999, ApJ, 524, 262
McKernan, B., Ford, K. E. S., & O'Shaughnessy, R. 2020, MNRAS, 498, 4088
McKinney, J. C., & Uzdensky, D. A. 2012, MNRAS, 419, 573
Meegan, C., Lichti, G., Bhat, P. N., et al. 2009, ApJ, 702, 791
Mészáros, P. 2006, RPPh, 69, 2259
Meszaros, P., & Rees, M. J. 1992, ApJ, 397, 570
Metzger, B. D., Quataert, E., & Thompson, T. A. 2008, MNRAS, 385, 1455
Mooley, K. P., Deller, A. T., Gottlieb, O., et al. 2018a, Natur, 561, 355
Mooley, K. P., Nakar, E., Hotokezaka, K., et al. 2018b, Natur, 554, 207
Murase, K., Asano, K., & Nagataki, S. 2007, ApJ, 671, 1886
Murase, K., Guetta, D., & Ahlers, M. 2016, PhRvL, 116, 071101
```

```
Murase, K., & Ioka, K. 2013, PhRvL, 111, 121102
Murase, K., Toma, K., Yamazaki, R., & Mészáros, P. 2011, ApJ, 732, 77
Murase, K., Toomey, M. W., Fang, K., et al. 2018, ApJ, 854, 60
Narayan, R., Paczynski, B., & Piran, T. 1992, ApJL, 395, L83
Nixon, C., King, A., & Price, D. 2013, MNRAS, 434, 1946
Norris, J. P., & Bonnell, J. T. 2006, ApJ, 643, 266
Ohsuga, K., Mineshige, S., Mori, M., & Kato, Y. 2009, PASJ, 61, L7
Paczynski, B. 1986, ApJL, 308, L43
Paczyński, B. 1998, ApJL, 494, L45
Perna, R., Lazzati, D., & Cantiello, M. 2021, ApJL, 906, L7
Popham, R., Woosley, S. E., & Fryer, C. 1999, ApJ, 518, 356
Rees, M. J., & Meszaros, P. 1994, ApJL, 430, L93
Rowlinson, A., O'Brien, P. T., Metzger, B. D., Tanvir, N. R., & Levan, A. J.
   2013, MNRAS, 430, 1061
Sadowski, A., Narayan, R., McKinney, J. C., & Tchekhovskoy, A. 2014,
   MNRAS, 439, 503
Sakamoto, T., Barthelmy, S. D., Baumgartner, W. H., et al. 2011, ApJS, 195, 2
Samsing, J., Bartos, I., D'Orazio, D. J., et al. 2020, arXiv:2010.09765
Savchenko, V., Ferrigno, C., Kuulkers, E., et al. 2017, ApJL, 848, L15
Tagawa, H., Haiman, Z., & Kocsis, B. 2020, ApJ, 898, 25
Tagawa, H., Kocsis, B., Haiman, Z., et al. 2021, ApJ, 908, 194
Tanikawa, A., Kinugawa, T., Yoshida, T., Hijikawa, K., & Umeda, H. 2021,
   MNRAS, 505, 2170
Troja, E., Piro, L., van Eerten, H., et al. 2017, Natur, 551, 71
Veres, P., & Mészáros, P. 2012, ApJ, 755, 12
Weaver, R., McCray, R., Castor, J., Shapiro, P., & Moore, R. 1977, ApJ,
  218, 377
Woosley, S. E. 1993, ApJ, 405, 273
Yang, Y., Bartos, I., Gayathri, V., et al. 2019a, PhRvL, 123, 181101
Yang, Y., Bartos, I., Haiman, Z., et al. 2019b, ApJ, 876, 122
Yang, Y., Gayathri, V., Bartos, I., et al. 2020, ApJL, 901, L34
Yuan, C., Murase, K., Kimura, S. S., & Mészáros, P. 2020, PhRvD, 102,
  083013
Yuan, C., Murase, K., Zhang, B. T., Kimura, S. S., & Mészáros, P. 2021,
  ApJL, 911, L15
Zhang, B. T., Murase, K., Veres, P., & Mészáros, P. 2021a, ApJ, 920, 55
Zhang, B. T., Murase, K., Yuan, C., Kimura, S. S., & Mészáros, P. 2021b,
   ApJL, 908, L36
Zhu, J.-P., Wang, K., & Zhang, B. 2021a, ApJ, 917, L28
Zhu, J.-P., Wang, K., Zhang, B., et al. 2021b, ApJL, 911, L19
Zhu, J.-P., Zhang, B., Yu, Y.-W., & Gao, H. 2021c, ApJL, 906, L11
```